PAPER

Check for updates

Programming hierarchical anisotropy in microactuators for multimodal actuation†

Shiyu Wang, [iD][a] Shucong Li,[b] Wenchang Zhao,[a] Ying Zhou,[a] Liqiu Wang,*[c]
Joanna Aizenberg [iD] *[de] and Pingan Zhu [iD] *[af]

Microactuators, capable of executing tasks typically repetitive, hazardous, or impossible for humans, hold great promise across fields such as precision medicine, environmental remediation, and swarm intelligence. However, intricate motions of microactuators normally require high complexity in design, making it increasingly challenging to realize at small scales using existing fabrication techniques. Taking inspiration from the hierarchical-anisotropy principle found in nature, we program liquid crystalline elastomer (LCE) microactuators with multimodal actuation tailored to their molecular, shape, and architectural anisotropies at (sub)nanometer, micrometer, and (sub)millimeter scales, respectively. Our strategy enables diverse deformations with individual LCE microstructures, including expanding, contracting, twisting, bending, and unwinding, as well as re-programmable shape transformations of assembled LCE architectures with negative Poisson's ratios, locally adjustable actuation, and changing from two-dimensional (2D) to three-dimensional (3D) structures. Furthermore, we design tetrahedral microactuators with well-controlled mobility and precise manipulation of both solids and liquids in various environments. This study provides a paradigm shift in the development of microactuators, unlocking a vast array of complexities achievable through manipulation at each hierarchical level of anisotropy.

Tribute to George Whitesides

For a special issue of Advanced Materials dedicated to George's 65th anniversary, I contributed a paper "Crystallization in patterns: a bio-inspired approach" (*Adv. Mater.* 2004, **16**, 1295), into which I encoded an acrostic with first letters of paragraphs reading "To George with affection". Honestly, the word 'affection' is insufficient to capture the impact that George had, has, and will continue to have on his scientific family. Being a post-doc with George in the mid 1990-ies left an immeasurable imprint on me as a scientist; I learned a lot about how a huge group can be managed effectively, how to spend your own precious time on the problems worth exploring, not just on extensions of already existing research, and how to remove from manuscripts "all the potent and novel words". The Whitesides group has always been a wonderful eclectic mix of highly talented people, and I have been in contact with many of them, all these years. What unites us is our shared experience with George, a brilliant scientist and mentor, and a very generous person. We are all deeply grateful to him. And I am sure everyone loves his humor, which is as great as his science! – Joanna Aizenberg

Introduction

Microactuators with the capability for active motion, sensing, and responsive behavior have a potential to lead to a surge of

[a] *Department of Mechanical Engineering, City University of Hong Kong, Hong Kong, China. E-mail: pingazhu@cityu.edu.hk*
[b] *Department of Mechanical Engineering, Massachusetts Institute of Technology, Cambridge, MA, USA*
[c] *Department of Mechanical Engineering, The Hong Kong Polytechnic University, Hong Kong, China. E-mail: liqiu.wang@polyu.edu.hk*
[d] *Department of Chemistry and Chemical Biology, Harvard University, Cambridge, MA, USA. E-mail: jaiz@seas.harvard.edu*
[e] *John A. Paulson School of Engineering and Applied Sciences, Harvard University, Cambridge, MA, USA*
[f] *Shenzhen Research Institute, City University of Hong Kong, Shenzhen, China*
† Electronic supplementary information (ESI) available. See DOI: https://doi.org/10.1039/d4lc00369a

development in various fields, including energy harvesting,[1,2] environmental remediation,[3,4] object manipulation,[5,6] and biomedicine.[7,8] These miniature mechanical systems, measuring millimeters or less in size, can navigate intricate and confined environments, such as gastrointestinal systems,[9,10] blood vessels,[11] and even cells.[12,13] However, achieving complex motion in these small machines requires high complexity in geometric shape,[5,6,14,15] material composition,[11,14,16,17] structural orientation,[6,18,19] and actuation methods.[15,20,21] This complexity may impose higher requirements in design, manufacturing, and manipulation of microactuators, potentially leading to increased risks of mechanical vulnerability and malfunctions. Therefore, it is crucial to develop microactuators with high complexity in functions while adhering to simple rules.

The sophisticated architectures found in many biological systems can be attributed to the integrated

anisotropies across multiple length scales.[22–24] In nature, remarkably complex shapes and patterns are created with anisotropies at different scales. Each level of anisotropy independently and synergistically provides, optimizes, and amplifies the functionality of the system, ultimately leading to complex and functional outcomes.[22,25–29] Octopuses, for instance, demonstrate intricately hierarchical anisotropic structures across scales (Fig. 1a), characterized by directional arrangement of muscle fibers in arm musculatures on a microscale and multiped shape of the body on a macroscale. These anisotropic orientations at various hierarchical levels enable the remarkable dexterity of octopuses, facilitating structural and functional changes.[27,28] While asymmetric or multi-material designs have been utilized in microactuators for gradient-triggered motion[30–33] and actuation,[34] these artificial machines show limited levels of structural and/or compositional anisotropies. Applying the hierarchical-anisotropy principle found in nature to develop artificial systems with advanced

functionality and enriched design remains to be fully explored.

Here we demonstrate that microactuators with multimodal actuation achieved by programming hierarchical anisotropy inspired by nature. Our strategy involves the precise engineering of anisotropic features at multiple scales using thermoresponsive liquid crystalline elastomer (LCE).[35–38] Anisotropic features are tailored individually at the molecular level for directional alignment of mesogens in LCE, at the microscale for anisotropic shape of LCE microstructures, and at the (sub)millimeter scale for arbitrary construction of architected LCE microactuators (Fig. 1b). This hierarchical design is achieved through a three-step fabrication process (Fig. 1c): firstly, mesogens within LCE are aligned along predetermined directions (Fig. S1†) via an external magnetic field;[36,39,40] secondly, the form of LCE microstructures is engineered by a soft manufacturing approach enabled by microfluidics;[32,41] and lastly, architected microactuators with well-defined size, shape, and configuration are created through tunable assembly of LCE
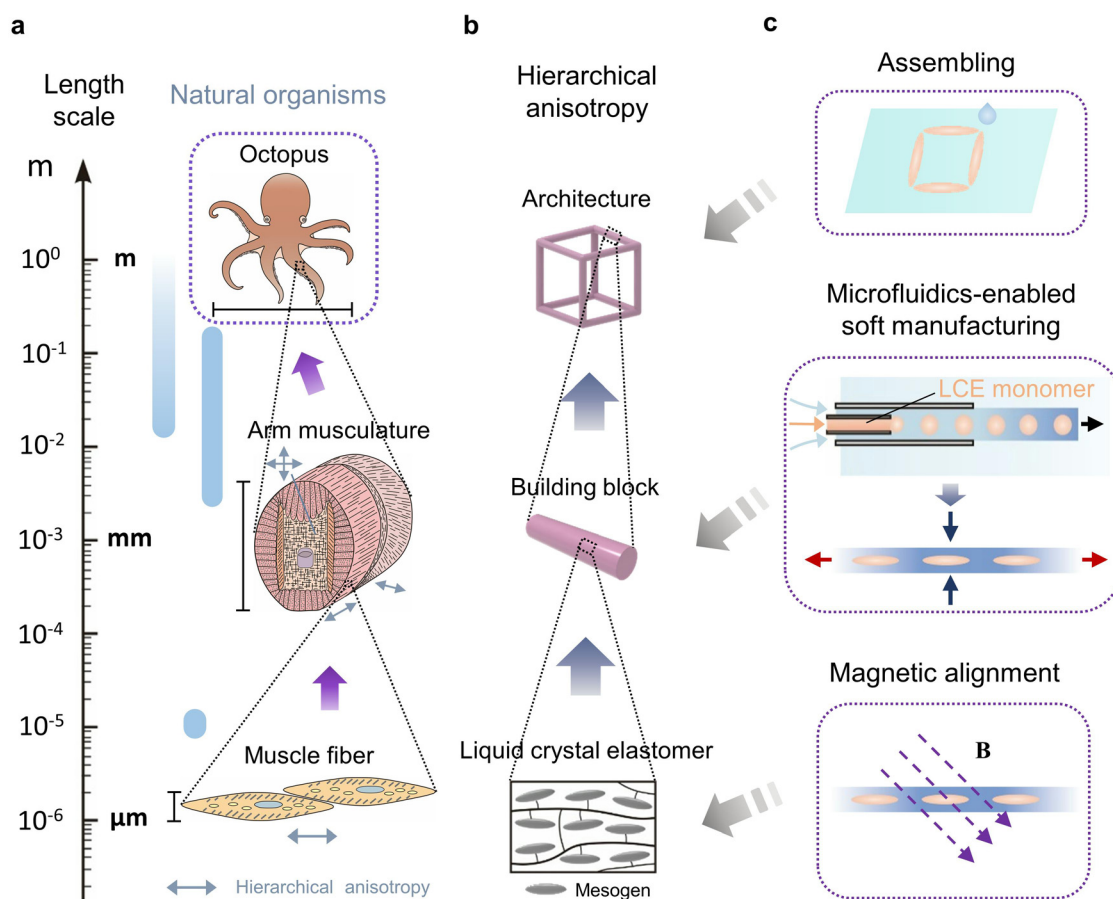

Fig. 1 Nature-inspired hierarchical anisotropy strategy. (a) A prototypical exemplar of high-performance natural architectures, the dexterous octopus exhibiting highly ordered structural orientations and anisotropies across distinct length scales. (b) Nature-inspired construction strategy: the synergy between the alignment anisotropy of mesogens, shape anisotropy of LCE building blocks, and architectural anisotropy of assembled structures enables the construction of diverse complex structures from a single material. (c) Multi-scale fabrication for independent engineering anisotropies at three distinct scales: the arrangement of mesogens is aligned in an arbitrary direction by magnetic fields; the dimension and shape of LCE microstructures are defined by the microfluidics-enabled soft manufacturing method; the configuration of high-order architectures is controlled by the assembly of LCE building blocks.

building blocks. While LCEs have been widely used in multimodal actuators/robots[42–49] ranging from centimeter to micrometer scales, our method offers more flexible designs and versatile actuation of LCE architectures by decoupling anisotropies at each level. We envision that our strategy is general and applicable to other stimuli-responsive materials, opening avenues for the development of sophisticated microactuators.

Results and discussion

Tuning the molecular anisotropy

LCEs are slightly cross-linked polymer networks that combine the molecular anisotropy of liquid crystals (LCs) with the rubber elasticity of polymer networks. These materials exhibit significant, reversible shape changes when exposed to external stimuli such as heat, light, electric and magnetic fields.[37,38,50–52] When heated above the nematic-to-isotropic transition temperature (T_{NI}), LCEs undergo an order–disorder transition of the LC phase, resulting in contraction along the direction of molecular alignment and expansion in the orthogonal directions.[35,50,53–55] At the molecular level, aromatic mesogen

units with a positive anisotropic magnetic susceptibility tend to align parallel to magnetic fields.[40] Thus, using magnetic field allows for the arbitrary orientation of the LC director within LCE microstructures prior to polymerization.

As an example, we use high-aspect-ratio micro-rods to show a variety of LCE deformations that can be achieved by solely tuning the orientation of mesogens (Fig. 2). Fig. 2a and b contrast optical micrographs between anisotropic and isotropic micro-rods under crossed polarizers, demonstrating the molecular alignment within the anisotropic micro-rod. We define the alignment angle (θ) of the mesogenic director (n) with respect to the longer axis of the slender micro-rod (*i.e.*, the Z-axis in Fig. 2c). Three representative deformations are anticipated with thermally actuated LCE micro-rods. At $\theta = 0°$ (Fig. 2c, i), the micro-rod is significantly compressed with a large contraction in its length along the Z-axis and a radial expansion of the cross-section in the X–Y plane. At $\theta = 90°$ (Fig. 2c, ii), the micro-rod is "squashed" when thermally actuated, with the deformation characterized by a slight increase or decrease (due to internal defects) in its length along the Z-axis, a notable contraction
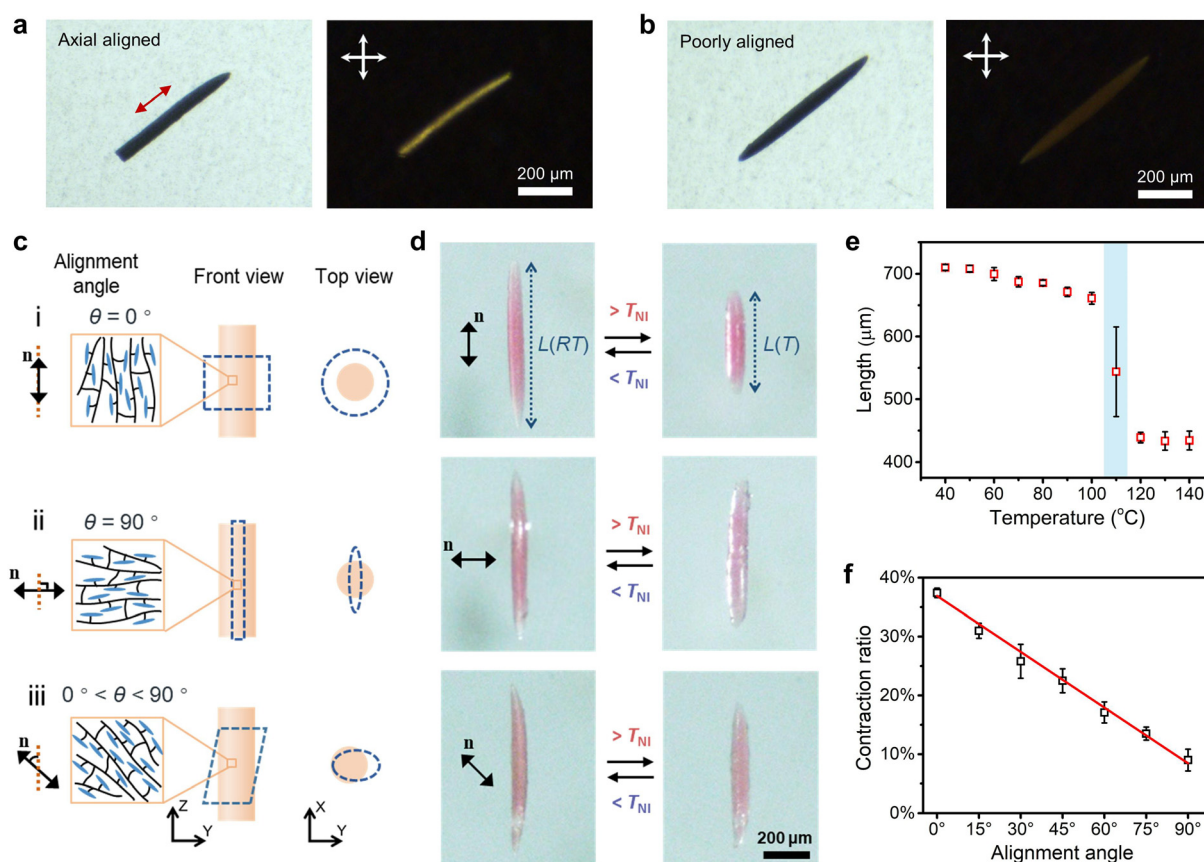

Fig. 2 Tunable thermoresponsive deformation of LCE micro-rods by regulatable alignment of mesogens. (a and b) White light (left) and polarized light (right) optical micrographs of (a) anisotropic and (b) isotropic LCE micro-rods. (c) Schematics showing various deformations of LCE micro-rods determined by the mesogenic director with different alignment angles (θ) with respect to the longer axis of the micro-rod. Panel (i) represents $\theta = 0°$, (ii) corresponds to $\theta = 90°$, and (iii) depicts $0° < \theta < 90°$. The blue dashed outlines indicate the deformed shapes of micro-rods. (d) Optical microscopy images displaying the nematic (left column) and isotropic (right column) states of LCE micro-rods with different mesogenic alignments. (e) The change in the final stable length of the LCE micro-rod *versus* temperature. (f) Tuning the contraction ratio of the LCE micro-rod by the alignment angle.

along the Y-axis, and an expansion along the X-axis. For intermediate orientations of mesogens ($0° < \theta < 90°$), the deformation is a combination of the two previous modes, with the extent of deformation determined and tunable by θ (Fig. 2c, iii). Fig. 2d shows reversible thermal deformations corresponding to the aforementioned three cases.

We have experimentally varied the alignment angle to assess the thermal actuation of LCE micro-rods. The final stable length of the micro-rod is plotted as a function of temperature in Fig. 2e with $\theta = 0°$. A small deformation occurs before 100 °C. However, a significant decrease in length can be observed between 100 °C and 120 °C, where the nematic–isotropic transition takes place. Above

120 °C, the length of the micro-rod will remain almost constant. A contraction ratio (α) is used to quantify the deformation of LCE micro-rods, defined as $\alpha = [L(RT) - L(T)]/L(RT) \times 100\%$, where $L(RT)$ and $L(T)$ indicate the length of the micro-rod at room temperature ($RT = 25$ °C) and a higher temperature ($T = 130$ °C), respectively. Fig. 2f shows the change of the contraction ratio α as a function of the alignment angle θ, which decreases linearly with increasing θ. For instance, the contraction ratio is ~37%, ~22%, and ~9% when θ is 0°, 45°, and 90°, respectively. These results demonstrate that tuning the orientation of mesogens provides a robust tool to control LCE deformation.[36]
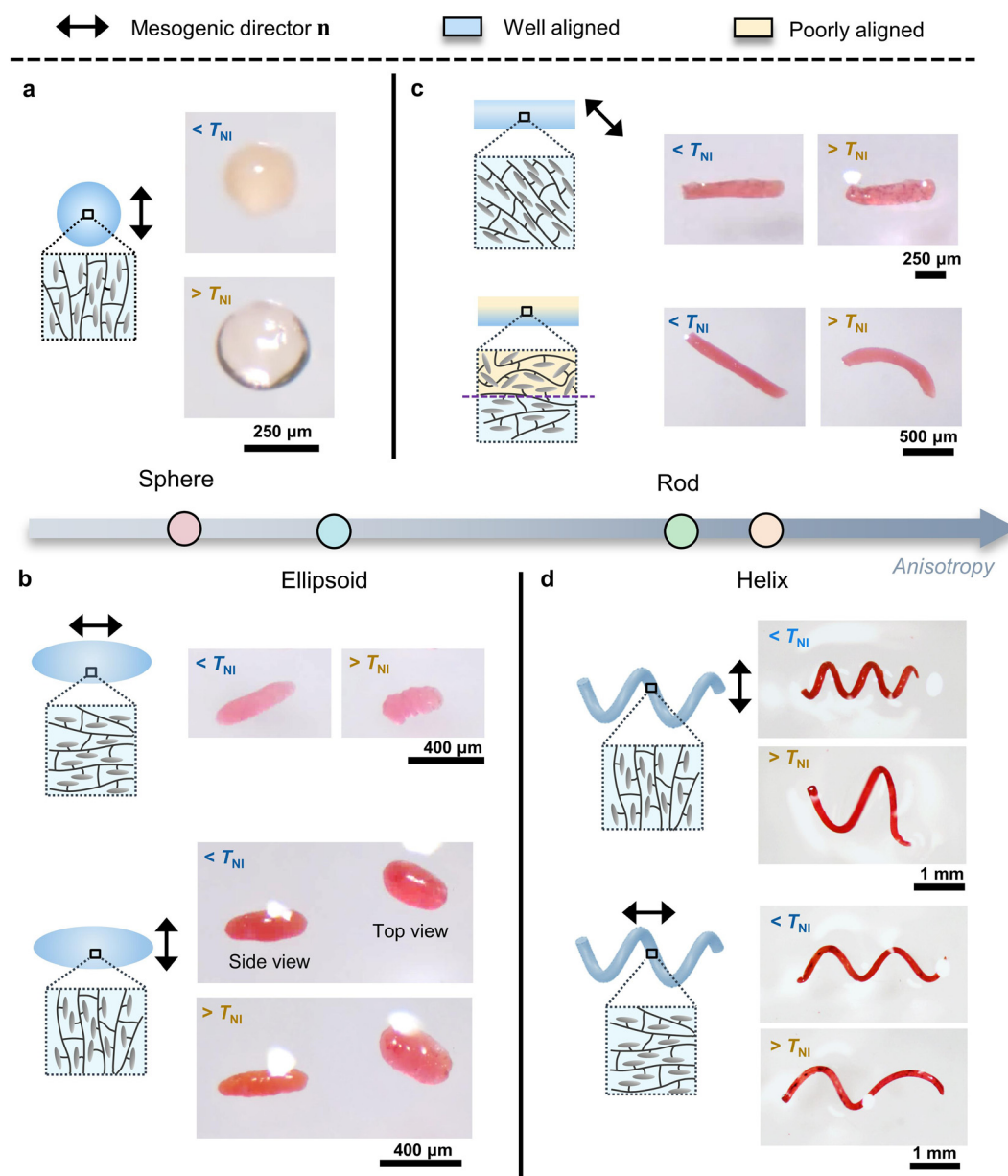

Fig. 3 Various deformations of LCE microstructures achieved by tailoring shape anisotropy. (a) Spherical LCE microparticles. (b) Ellipsoidal LCE microparticles with an alignment angle of 0° (up) and 90° (bottom). (c) LCE micro-rods with an alignment of 45° (up) and a gradient in the alignment of mesogens (bottom). (d) Helical LCE microfibers with an alignment angle of 90° (up) and 0° (bottom).

Engineering the shape anisotropy

The fabrication of LCE microstructures with tunable anisotropic shapes further enhances the complexity of deformation (Fig. 3), as achieved by a modified microfiber-confined method,[32,33,41] with more details included in Note S1.† We used a co-flow microfluidic device to create oil-core/hydrogel-shell microfibers, with the microfiber shell acting as a dynamic template (Fig. S2 and S3†). The dehydration-induced radial shrinkage of the fiber shell compressed the spherical core droplets into an ellipsoid or elongated shape (Fig. S4 and S5†). Further squeezing of the droplets resulted in rod-like shapes with higher aspect ratios (Fig. S6 and S7†). After drying, the deformed oil cores were crosslinked to produce LCE microstructures of anisotropic shapes. This method allowed us to produce elongated LCE microfibers when the inner oil formed a continuous liquid jet inside the hydrogel microfiber. We fabricated a more complex spatial structure by rolling the LCE microfiber along a cylindrical rod (Fig. S3d†). The cross-section of the produced LCE material can also be made anisotropic, as demonstrated by the ribbon-like microstructures (Fig. S6†). These results demonstrate a wide range of anisotropic LCE materials at the microscale.

We created a variety of 3D LCE microstructures with coordinated anisotropies at both the molecular and microscale levels to demonstrate the increased complexity of deformation (Fig. 3). The microscale shape anisotropy is characterized by the aspect ratio of the microstructure, which starts from unity for the spherical shape and increases steadily for the ellipsoidal, rod-like, and helical shapes. Note that the deformation of the isotropic microsphere is limited to only one mode with a transformation between the spherical and the pancake-like shape regardless of the mesogenic director (Fig. 3a and Movie S1†).

In comparison, the anisotropic LCE microstructures show more complex deformations (Movie S2†), such as expansion and contraction on different sides of the LCE micro-ellipsoid (Fig. 3b) and twisting of the LCE micro-rod (Fig. 3c) when the alignment of mesogens is engineered. Furthermore, a gradient in the molecular alignment leads to heterogeneous deformation in the LCE micro-rod for bending actuation, where mesogens are well-aligned on one side of the micro-rod but have a lower order parameter on the other side (Fig. 3c and Movie S3†). This bending deformation can be used to drive the movement of an LCE micro-rod when the friction between the micro-rod and the solid surface is different at the two ends (Fig. S8†).

The coordinated anisotropies are further demonstrated in helical microfibers with a recurrent distribution of the anisotropic mesogenic orientation along the main geometric axis of the LCE fiber, which allows unwinding deformation at temperatures above T_{NI} (Fig. 3d and Movie S4†). It is worth noting that the extent of structure expansion by unwinding is significantly affected by the direction of the molecular alignment, highlighting the major role of coordinated anisotropies in designing complex shape transformations of LCE microstructures.

The original shape of LCE microstructures is further adjustable by the shape memory effect (Fig. S9†). When heated to a temperature T where $T_{NI} > T > T_g$ (T_g being the glass transition temperature of LCE), the LCE is soft enough to be temporarily reshaped into any form while keeping the molecular alignment. The temporary shape is kept by cooling the LCE below the glass transition temperature and erased by heating the LCE above T_g again, which allows for the reprogramming of the shape. Due to the unchanged mesogenic alignment, the reshaped LCE will be transformed into the same actuated shape when heated above T_{NI}. This shape memory effect can provide a variety of shape anisotropies for LCE microstructures with numerous possibilities.

Assembled anisotropic architectures

Leveraging the diverse deformations of LCE microstructures, we used them as building blocks to construct higher-order architectures with more complex transformations by engineering architectural anisotropy at the (sub)millimeter scale. This allows for an additional synergy between shape deformation and mesogenic orientation of individual building blocks, even with two LCE microspheres that only have one way of deformation (Fig. S10†). Utilizing anisotropic LCE building blocks significantly increases the diversity of architectural transformations. To demonstrate this, we assembled anisotropic LCE micro-rods into several types of higher-order architectures (Fig. 4).

For example, square-frame machines were constructed to show various topological changes from the same initial geometry. By assembling LCE building blocks with different molecular anisotropy, the square frames can display isotropic contraction into a smaller square frame (Fig. 4a), anisotropic contraction into a rectangular frame (Fig. 4b), and even frame bending into a circular shape (Fig. 4c) when thermally actuated. The actuated square frames exhibit negative Poisson's ratio (Movie S5†), where the enclosed area of the frame decreases when the frame is heated above the T_{NI} and restores the initial value when the frame is cooled down (Fig. 4d). Notably, this negative Poisson's ratio is achieved with a simple geometric configuration instead of complex structural designs of metamaterials. Fig. 4e illustrates the remarkable stability of the actuation for assembled structures after multiple deformation-recovery cycles.

Similarly, a square-wave-shaped structure was created by alternating LCE micro-rods with well-aligned and poorly-aligned mesogens, demonstrating the ability to produce local deformations (Fig. 4f and Movie S6†). When actuated, the amplitude of the square-wave architecture is altered while the periodicity of the architecture remains nearly constant (Fig. 4f), which can be further customized by engineering the mesogenic alignment and the spatial arrangement of LCE building blocks.
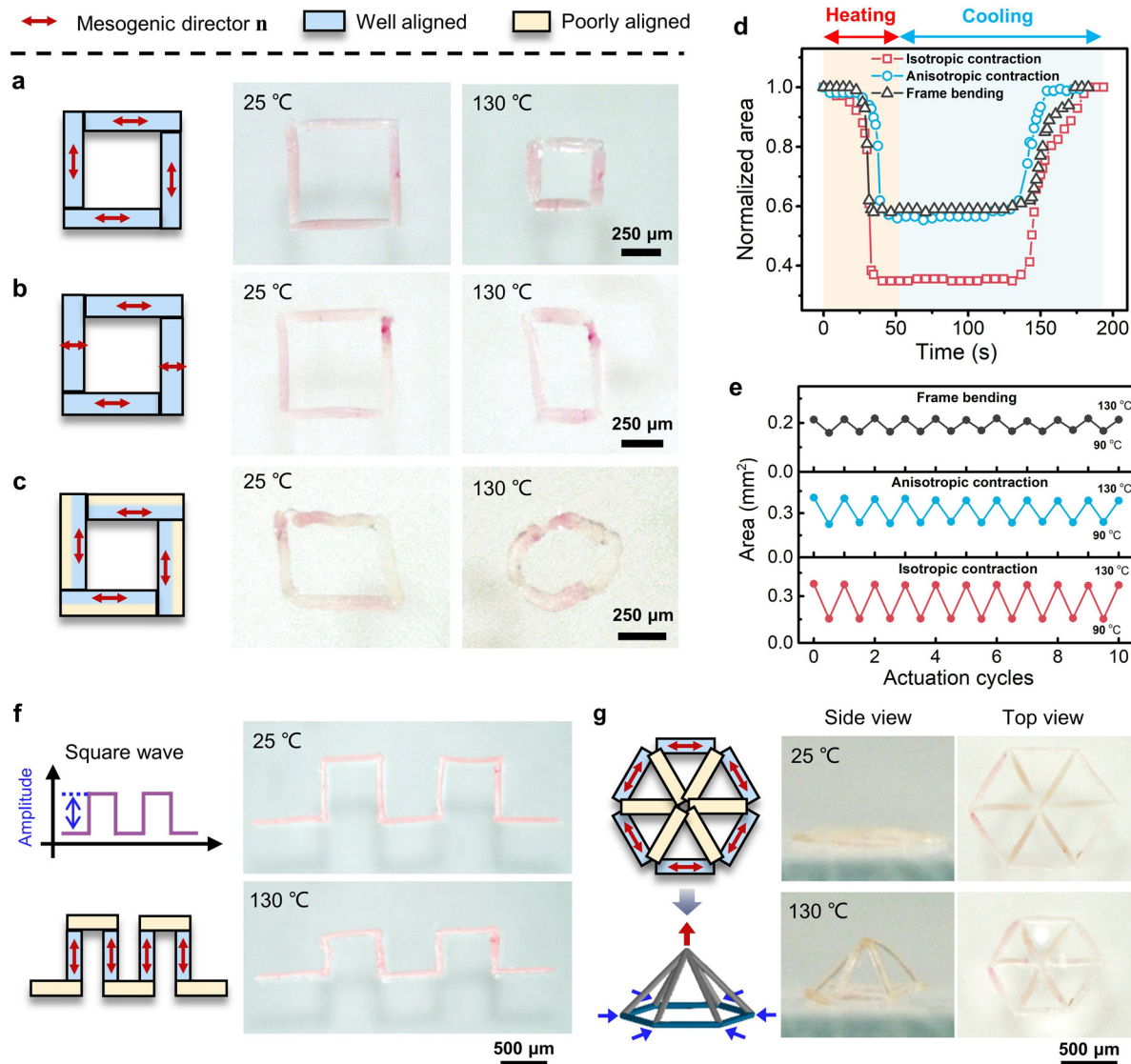
Fig. 4 Thermoresponsive LCE architectures demonstrating diverse deformations. (a–c) Square-frame LCE architectures with three different configurations, exhibiting isotropic contraction (a), anisotropic contraction (b), and bending actuation (c). (d) Variations of the square-frame encompassed area (normalized by the initial area) with time by heating and cooling. (e) Evolution of the area of the LCE frame during ten actuation cycles, demonstrating the robust stability and full reversibility of the shape change of assembled LCE architectures. (f) An assembled square-wave structure displaying a transformation of varied amplitude but constant period. (g) An assembled hexagonal wheel demonstrating a shape change from a 2D to a 3D configuration.

Lastly, we demonstrated the transformation from 2D to 3D configurations by constructing a hexagonal wheel with six spokes (Fig. 4g and Movie S7†). The assembled architecture consists of twelve LCE micro-rods, six of which form spokes without deformation, and another six constitute edges with contraction deformation along the longer axis. As edges contract in length, the spokes are forced to undergo an out-of-plane reconfiguration due to the limited degree of freedom. As a result, the architected wheel bulges up vertically from the initial 2D flat shape to form a final 3D hexagonal pyramid with the bottom hexagonal frame shrinking homogeneously when heated from 25 °C to 130 °C (Fig. 4g). Note that the transformation of assembled architectures can be further diversified by

independently customizing anisotropies at the three hierarchical levels.

Tetrahedral microactuators for controllable locomotion

We developed magnetic LCE microactuators by equipping the assembled architectures with magnetically controllable locomotion. The microactuator is in the shape of a regular tetrahedron, which makes it naturally suitable for effective motion in different directions. Fig. 5a shows a prototype of the microactuator composed of LCE edges (with a characteristic length of ~850 μm) and Fe_3O_4 microbead vertices. When a continuously rotating magnetic field is applied, the force on the four magnetic vertices can cause
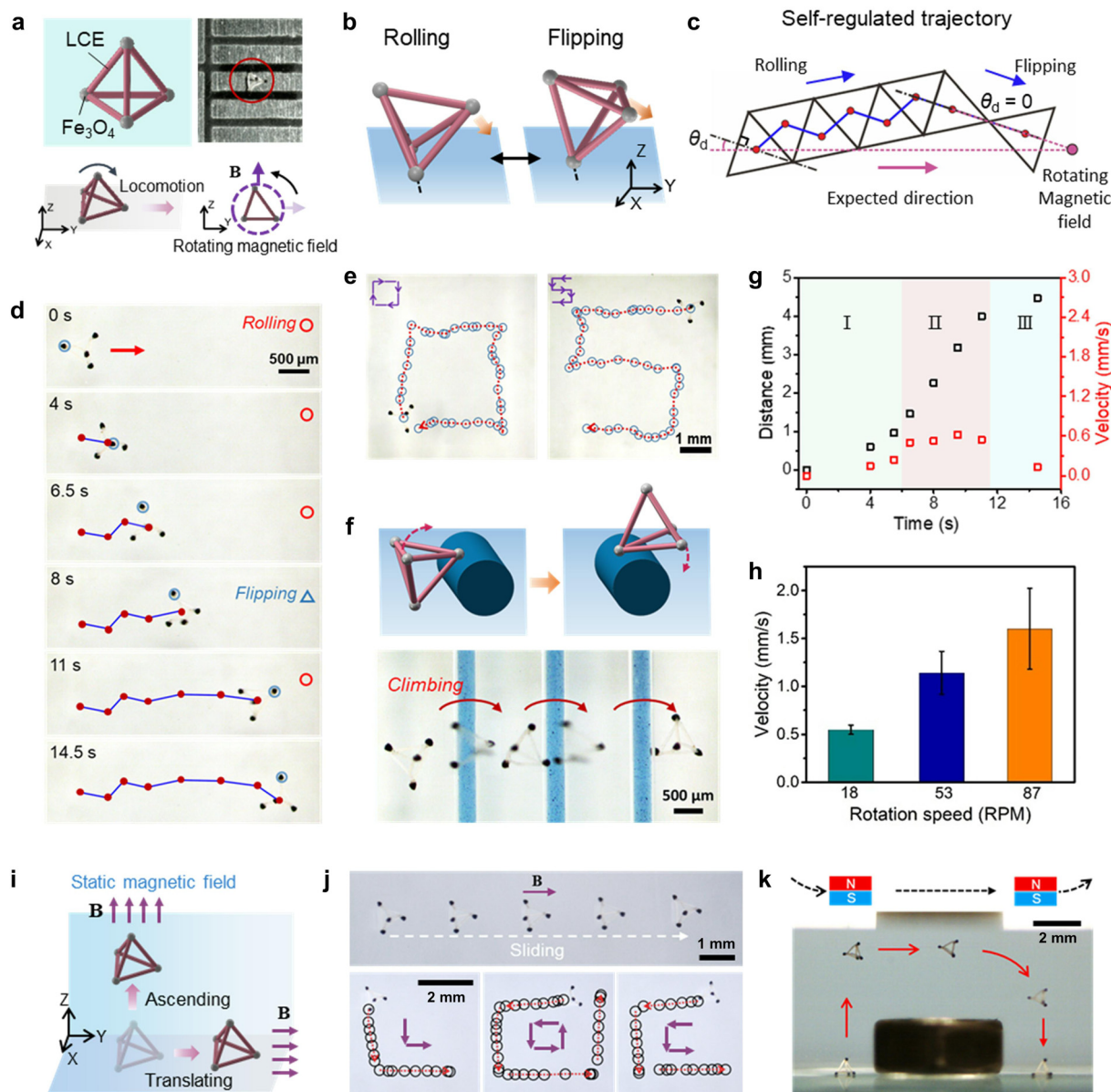
Fig. 5 Architected LCE microactuators with well-controlled mobility. (a) Tetrahedral LCE microactuators incorporating magnetic microbeads at vertices for the motion actuated by a rotating magnetic field. (b) Rolling and flipping modes of locomotion. (c and d) Schematic (c) and experimental observation (d) showing the process of self-regulated locomotion by a switch from the rolling to the flipping mode. (e) Magnetically guided motion of the microactuator along predetermined trajectories. (f) The microactuator climbing over obstacles. (g) The three-stage variation in the locomotion distance and velocity of the microactuator with time. (h) Controlling the motion velocity of the microactuator by the rotation speed of the magnetic field. (i) A schematic showing the microactuator's response to a static magnetic field. (j) Top: The translational motion of the microactuator actuated by a static magnetic field. Bottom: The manipulation of the microactuator along designed locomotion paths by changing the direction of the static magnetic field. (k) The microactuator flying over an obstacle in silicone oil under magnetic control.

the entire structure to rotate, allowing it to move. The motion of the tetrahedral microactuator has two modes, depending on the interaction between its geometric features and the terrain: rolling around an edge and spinning around a vertex (Fig. 5b).

The microactuator can spontaneously adjust its motion trajectory by combining the rolling and flipping modes (Fig. 5c and Movie S8†). Usually, the axis of symmetry of the triangular base of the tetrahedral microactuator is not

parallel to the direction of motion, but instead forms a deflection angle θ_d (Fig. 5c), which causes the motion trajectory to deviate from the expected direction. However, the deflection angle gradually decreases with the continuous rolling motion, eventually reaching zero or a value close to zero, at which point the motion mode switches to flipping (Fig. 5c). The change in the motion mode causes the motion trajectory to be corrected spontaneously, which has been confirmed by experimental observation (Fig. 5d). This self-

regulated locomotion endows the tetrahedral microactuator with robust motion stability and improved resilience to changes that may cause trajectory deviations, such as disturbances from the environment, uneven terrains, and defects in the symmetry of architecture design.

Fig. 5e shows that the self-adaptive switch between the two motion modes enables the tetrahedral microactuator to move along predefined complex trajectories, such as a square-shaped path and an "S"-shaped path (Movie S9†). The two motion modes also allow the microactuator to climb over obstacles with a height comparable to its size (Fig. 5f and Movie S10†), making it adaptive to environments with complicated terrains. The motion speed of the microactuator displays a three-stage variation (Fig. 5g): acceleration (I), constant speed (II), and deceleration (III). The average speed is controlled by the rotation speed of the magnetic field, which is on the order of millimeters per second (Fig. 5h).

Compared to a rotating magnetic field, a static magnetic field offers simpler and more effective manipulation of the microactuator with superior directional control, especially
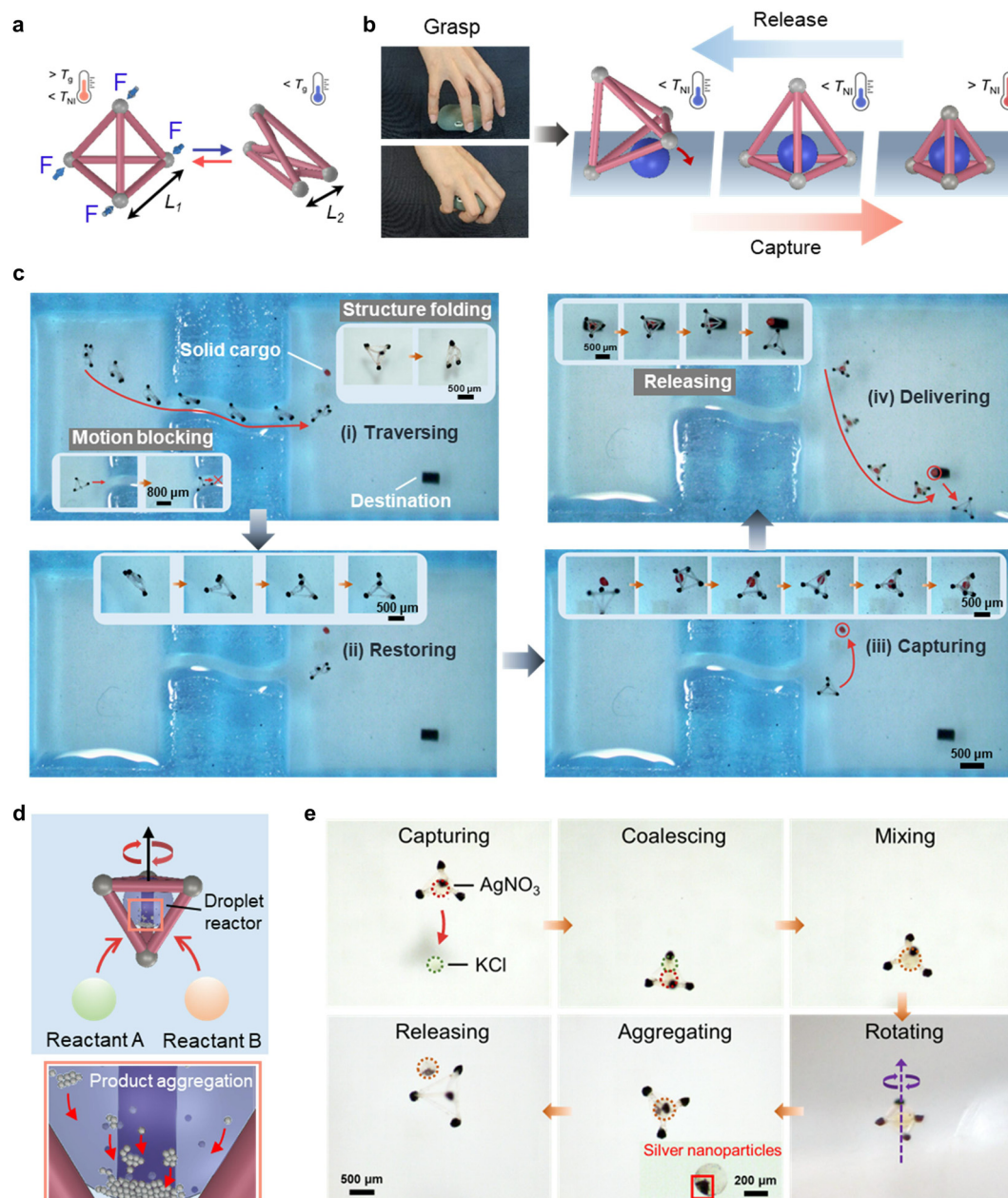

Fig. 6 Manipulation of matter by architected LCE microactuators. (a) Temporary transformation of the microactuator by the shape memory effect of LCE. (b) Schematics of cargo capture and release by the thermally actuated change in the volume of the microactuator. (c) The microactuator performing complex tasks of passing through a narrow channel (i), recovering the initial shape (ii), capturing a solid cargo (iii), and releasing the cargo after delivering it to the target (iv). (d and e) Schematics (d) and snapshots (e) showing the on-demand chemical reaction enabled by the microactuator capable of manipulating liquid microdroplets.

when it is positioned on a smooth surface (Fig. 5i–k). As shown in Fig. 5j and Movie S11,† when subjected to a static magnetic field in the horizontal direction, the microactuator readily slides in a translational manner, resulting in more precise motion along various trajectories than those achieved by a rotating magnetic field. Moreover, microactuators are maneuverable in a liquid environment as well as in air. For example, placing the magnetic field above a microactuator allows for controlling its height and guiding it to fly over an obstacle much larger than its size (Fig. 5k and Movie S12†).

Manipulation of solids and liquids

We now focus on applications of tetrahedral LCE microactuators in the manipulation of different materials under various conditions. The shape memory ability imparts foldability to the microactuator for fitting into confined geometry (Fig. 6a); the reversible shape transformation endows the microactuator with negative Poisson's ratio for cargo capture and release, mimicking the function of fingers (Fig. 6b); the magnetic-driven locomotion allows the microactuator to deliver and process different materials.

We demonstrate the manipulation of a solid cargo using the tetrahedral LCE microactuator placed in a chamber with a geometrically confined microchannel (Fig. 6c and Movie S13†). The microactuator is folded into a squashed structure with a reduced dimension to pass through the microchannel (Fig. 6c, i). After that, the microactuator is unfolded to recover the initial structure when heated above T_g (Fig. 6c, ii). The microactuator is designed to reduce the size of the tetrahedral cage when actuated above T_{NI}, which captures and firmly traps the solid cargo in the shrunken cage (Fig. 6c, iii). The cargo is released by the microactuator *via* a reversible transformation after the delivery to the destination (Fig. 6c, iv). The microactuator has the capacity to traverse rough terrains and climb over obstacles (Fig. S11†). It can also accurately capture, deliver, and release cargos, allowing it to carry out complex tasks in complex environments, such as the gastrointestinal system and blood vessels for biomedical applications.

Furthermore, the tetrahedral microactuator can manipulate liquid droplets to complete chemical reactions for material synthesis (Fig. 6d). As an example, Fig. 6e and Movie S14† show the chemical reaction between $AgNO_3$ and KCl microdroplets in the cage-like LCE tetrahedron. The two microdroplets are sequentially captured by the thermally-actuated microactuator and then coalesce to mix the two reagents. The product is then collected at the bottom of the droplet microreactor by rotating the microactuator magnetically for centrifugation. When exposed to light, the initially generated AgCl decomposes to form silver nanoparticles as the final product (Fig. 6e). This tetrahedral microactuator combines multiple functions, such as deft transport of droplets, efficient mixing of reagents, and rapid centrifugation of products, which could be beneficial for chemical/biological applications.

Conclusion

We have shown how complexity can be derived from simple design principles to create advanced artificial systems. Leveraging this concept, we have designed architected microactuators with complex transformations and functions by programming their molecular, shape, and architectural anisotropies at the nanometer, micrometer, and (sub) millimeter scales, respectively. Combining the anisotropies from different levels leads to a substantial increase in shape transformations. Altering the synergy between levels provides a simple route for re-programming the shape and structure of the designed architectures.

We have created tetrahedrally architected LCE microactuators with shape memory effect, magnetic responsiveness, and thermal actuation, allowing them to keep temporary shapes, self-regulate their motion trajectories, and undergo programmable shape transformations, respectively. These microactuators can perform complex tasks such as on-the-fly capture, targeted delivery, and on-demand release of solid cargos while navigating in confined spaces. They can also manipulate liquid droplets, enabling complex chemical reactions. These results show that the architected microactuators can manipulate different materials in various complex environments due to their tailorable hierarchical anisotropy, making them suitable for a variety of applications.

This strategy promises even more advances in artificial systems by increasing the number of hierarchical levels. For example, photoresponsive LCEs not only facilitate dynamic anisotropy for extended deformations and applications[36,56,57] but also offer a solution to the high-temperature requirements demonstrated in the thermal deformation, making them suitable for biomedical applications.[20,58] Additionally, the incorporation of multiple materials and/or multi-stimuli-responsive materials will enable architectures with complex structures and configurations.[6,16] Furthermore, the deformation of architectures can be accurately predicted through numerical modeling, providing proactive guidance for the customized implementation of specific functionalities.[36,56,57] Our strategy of hierarchically engineering anisotropy is general and has broad applicability to other systems, opening up vast opportunities for the development of advanced actuators and materials in the near future.

Materials and methods

Materials

The LC monomer, 4″-acryloyloxybutyl 2,5-di(4′-butyloxybenzoyloxy)benzoate, was synthesized using a procedure described in a previous study.[35] The following materials were purchased and used upon received: 1,6-hexanediol diacrylate, 2-hydroxy-2-methylpropiophenone, dichloromethane (DCM, Dieckmann, AR), sodium alginate (Aladdin), paraffin oil (Macklin), tetrasodium

ethylenediaminetetraacetate dehydrate (EDTA-4Na, Macklin), calcium chloride ($CaCl_2$, Aladdin), poly(vinyl alcohol) (PVA, 87–89% hydrolyzed, Aladdin), bonding agent (Ergo 8500, Kisling), distilled water (Watsons), fluorinated oil (Krytox GPL-105, DuPont), silicone oil (viscosity of 1 mPa s, Aladdin), Fe_3O_4 microbeads (Zhong Hang Zhong Mai Materials), $AgNO_3$ (Acros), KCl (Meryer), and rhodamine 6G (95%, Aladdin).

Fabrication of microfluidic devices

Co-flow microfluidic devices were fabricated by coaxially aligning a cylindrical glass capillary (with an inner diameter of 100 μm) in an outer one (with an inner diameter of 900 μm). The outlet of the outer glass capillary was inserted into a plastic Petri dish filled with a 6 wt% aqueous solution of calcium chloride.

Fabrication of droplet-encapsulating microfibers

A mixture of LC monomer 4″-acryloyloxybutyl 2,5-di(4′-butyloxybenzoyloxy)benzoate, cross-linker 1,6-hexanediol diacrylate (5% wt/wt based on LC monomer), and photo-initiator 2-hydroxy-2-methylpropiophenone (2% wt/wt based on LC monomer) was dissolved in DCM, which was used as the inner phase liquid. A red dye (rhodamine 6G, 0.1 wt%) was added to the inner phase liquid for better visualization. The outer phase liquid was an aqueous solution of sodium alginate (NaAlg, 2 wt%). The two liquids were pumped into the microfluidic device by high-precision syringe pumps (Longer Pump, LSP01-1A). The inner phase liquid was disintegrated into oil droplets by the outer phase liquid in the co-flow microchannel and then spontaneously ordered into a one-dimensional (1D) droplet array. Hydrogel microfibers, which encapsulated the oil droplet array, were generated by solidifying the NaAlg with $CaCl_2$ *via* ionic crosslinking when the outer phase liquid flowed out of the capillary outlet into the Petri dish. The produced hydrogel microfibers were then hung vertically to dry in the air and shrunk radially, thus deforming the encapsulated oil droplets into anisotropic shapes. During the drying process, DCM gradually evaporated out of the oil droplet, which transformed liquid droplets into solid particles containing only the LC monomer mixture. By tuning the flow rates of the two liquids, the inner phase liquid can form continuous liquid jets instead of discrete droplets, which were used as templates to produce LCE microfibers after polymerization.

Magnetic alignment of mesogens

The alignment of mesogens was conducted along with the polymerization of LC monomer. The dried hydrogel microfibers were first heated to 90 °C for 30 min so that the encapsulated LC-monomer particles were in the isotropic phase to clear any memory effect. Then the temperature was decreased to 60 °C for the alignment of mesogens under a magnetic field generated by a permanent magnet (~316 mT, NdFeB), during which polymerization was carried out by the UV light irradiation (light intensity = 95 mW cm^{-2},

wavelength λ = 365 nm) for 60 min. The axial direction of the hydrogel microfibers was tuned in the magnetic field to tailor the mesogenic director of LCE microstructures. The whole process was conducted by immersing the hydrogel microfibers in paraffin oil in a glass container. After polymerization, an aqueous solution of EDTA-4Na (2 wt%) was used to dissolve the alginate shell of the hydrogel microfibers for releasing the encapsulated LCE microstructures, which were then washed, dried, collected, and stored for experiments.

Assembly of LCE building blocks

To create LCE architectures, individual LCE building blocks were glued with each other by a bonding agent (Ergo 8500). Before assembly, the building blocks were temporarily stuck on a glass substrate to form predetermined 2D patterns by depositing a small amount of the aqueous PVA solution (2 wt%) on the contact area between LCE and the substrate. Next, a tiny drop of Ergo 8500 was gently dripped to the joint gap between neighboring LCE building blocks. The bonding agent spontaneously filled the gap by the capillary effect and then was cured by exposure to a UV light for 3 min. Finally, PVA was washed with distilled water to release the assembled architecture. To construct 3D architectures, 2D structures were first assembled and then folded into the desired 3D structures, followed by gluing all remaining joint gaps.

Thermal actuation

To observe the shape changes the LCE samples were tempered on a hot plate at 130 °C and cooled down from the isotropic to the nematic state by natural convection cooling. A high-density fluorinated oil was employed as matrix to ensure uniform heating over the whole structure and prevent hindered deformation caused by surface friction.

Magnetic actuation

The tetrahedral cage-like microactuator was navigated in a PDMS chamber filled with fluorinated oil or silicone oil to reduce the friction between the microactuator and the substrate for better locomotion (Fig. 6). A permanent magnet was connected to and rotated by an electric motor to generate a rotating magnetic field in the working space, which was used to actuate the rolling and flipping motions of microactuators. Besides, the magnet was also horizontally moved to control the translational motion of microactuators.

Characterization

Optical microscopy images and videos were captured by a stereomicroscope (SOPTOP SZM7045) equipped with a CMOS camera (SOPTOP OD-300). Polarized optical images were captured by an inverted microscope (Nikon ECLIPSE Ts2) equipped with crossed polarizers.

Data availability

The data supporting this article have been included as part of the ESI.†

Author contributions

S. W.: writing – original draft, visualization, methodology, investigation, formal analysis, data curation. S. L.: resources. W. Z.: investigation. Y. Z.: investigation. L. W.: conceptualization, supervision, funding acquisition. J. A.: conceptualization, supervision, funding acquisition. P. Z.: writing – review & editing, supervision, conceptualization, methodology, investigation, visualization, project administration, funding acquisition.

Conflicts of interest

Authors declare that they have no competing interests.

Acknowledgements

References

1 T. Ghomian and S. Mehraeen, *Energy*, 2019, **178**, 33–49.
2 Y. Wang, M. Dai, H. Wu, L. Xu, T. Zhang, W. Chen, Z. Wang and Y. Yang, *Nano Energy*, 2021, **90**, 106499.
3 W. Gao and J. Wang, *ACS Nano*, 2014, **8**, 3170–3180.
4 M. Urso, M. Ussia, F. Novotny and M. Pumera, *Nat. Commun.*, 2022, **13**, 3573.
5 E. Diller and M. Sitti, *Adv. Funct. Mater.*, 2014, **24**, 4397–4404.
6 J. Zhang, Z. Ren, W. Hu, R. H. Soon, I. C. Yasa, Z. Liu and M. Sitti, *Sci. Robot.*, 2021, **6**, eabf0112.
7 J. Li, B. Esteban-Fernandez de Avila, W. Gao, L. Zhang and J. Wang, *Sci. Robot.*, 2017, **2**, eaam6431.
8 S. Fusco, M. S. Sakar, S. Kennedy, C. Peters, R. Bottani, F. Starsich, A. Mao, G. A. Sotiriou, S. Pane, S. E. Pratsinis, D. Mooney and B. J. Nelson, *Adv. Mater.*, 2014, **26**, 952–957.
9 Q. Ze, S. Wu, J. Dai, S. Leanza, G. Ikeda, P. C. Yang, G. Iaccarino and R. R. Zhao, *Nat. Commun.*, 2022, **13**, 3118.
10 H. Lu, M. Zhang, Y. Yang, Q. Huang, T. Fukuda, Z. Wang and Y. Shen, *Nat. Commun.*, 2018, **9**, 3944.
11 Y. Kim, G. A. Parada, S. Liu and X. Zhao, *Sci. Robot.*, 2019, **4**, eaax7329.
12 A. Elbourne, S. Cheeseman, P. Atkin, N. P. Truong, N. Syed, A. Zavabeti, M. Mohiuddin, D. Esrafilzadeh, D. Cozzolino, C. F. McConville, M. D. Dickey, R. J. Crawford, K. Kalantar-Zadeh, J. Chapman, T. Daeneke and V. K. Truong, *ACS Nano*, 2020, **14**, 802–817.
13 D. Wang, C. Gao, W. Wang, M. Sun, B. Guo, H. Xie and Q. He, *ACS Nano*, 2018, **12**, 10212–10220.
14 X. Hu, I. C. Yasa, Z. Ren, S. R. Goudu, H. Ceylan, W. Hu and M. Sitti, *Sci. Adv.*, 2021, **7**, eabe8436.
15 S. Tottori, L. Zhang, F. Qiu, K. K. Krawczyk, A. Franco-Obregon and B. J. Nelson, *Adv. Mater.*, 2012, **24**, 811–816.
16 F. Soto, E. Karshalev, F. Zhang, B. E. F. de Avila, A. Nourhani and J. Wang, *Chem. Rev.*, 2022, **122**, 5365–5403.
17 J. Li and M. Pumera, *Chem. Soc. Rev.*, 2021, **50**, 2794–2838.
18 W. Hu, G. Z. Lum, M. Mastrangeli and M. Sitti, *Nature*, 2018, **554**, 81–85.
19 H. Gu, Q. Boehler, H. Cui, E. Secchi, G. Savorana, C. De Marco, S. Gervasoni, Q. Peyron, T. Huang, S. Pane, A. M. Hirt, D. Ahmed and B. J. Nelson, *Nat. Commun.*, 2020, **11**, 2637.
20 S. Palagi, A. G. Mark, S. Y. Reigh, K. Melde, T. Qiu, H. Zeng, C. Parmeggiani, D. Martella, A. Sanchez-Castillo, N. Kapernaum, F. Giesselmann, D. S. Wiersma, E. Lauga and P. Fischer, *Nat. Mater.*, 2016, **15**, 647–653.
21 A. Mourran, H. Zhang, R. Vinokur and M. Moller, *Adv. Mater.*, 2017, **29**, 1604825.
22 P. Fratzl and R. Weinkamer, Nature's hierarchical materials, *Prog. Mater. Sci.*, 2007, **52**, 1263–1334.
23 Z. Liu, Z. Zhang and R. O. Ritchie, *Adv. Funct. Mater.*, 2020, **30**, 1908121.
24 E. T. Roche, R. Wohlfarth, J. T. Overvelde, N. V. Vasilyev, F. A. Pigula, D. J. Mooney, K. Bertoldi and C. J. Walsh, *Adv. Mater.*, 2014, **26**, 1200–1206.
25 R. M. Erb, R. Libanori, N. Rothfuchs and A. R. Studart, *Science*, 2012, **335**, 199–204.
26 F. Barthelat, Z. Yin and M. J. Buehler, *Nat. Rev. Mater.*, 2016, **1**, 16007.
27 C. Laschi, B. Mazzolai, L. Margheri, M. Follador and P. Dario, *Adv. Robot.*, 2012, **26**, 709–727.
28 W. M. Kier and M. P. Stella, *J. Morphol.*, 2007, **268**, 831–843.
29 R. M. Erb, J. S. Sander, R. Grisch and A. R. Studart, *Nat. Commun.*, 2013, **4**, 1712.
30 W. Wang, L. A. Castro, M. Hoyos and T. E. Mallouk, *ACS Nano*, 2012, **6**, 6122–6132.
31 S. Zhu, W. Zheng, J. Wang, X. Fang, L. Zhang, F. Niu, Y. Wang, T. Luo, G. Liu and R. Yang, *Lab Chip*, 2022, **22**, 3412–3423.
32 C. Zhou, P. Zhu, Y. Tian, M. Xu and L. Wang, *ACS Nano*, 2019, **13**, 6319–6329.
33 P. Zhu, R. Chen, C. Zhou, M. Aizenberg, J. Aizenberg and L. Wang, *Adv. Mater.*, 2021, **33**, e2008558.
34 J. Kim, S. E. Chung, S. E. Choi, H. Lee, J. Kim and S. Kwon, *Nat. Mater.*, 2011, **10**, 747–752.
35 D. L. Thomsen, P. Keller, J. Naciri, R. Pink, H. Jeon, D. Shenoy and B. R. Ratna, *Macromolecules*, 2001, **34**, 5868–5875.
36 Y. Yao, J. T. Waters, A. V. Shneidman, J. Cui, X. Wang, N. K. Mandsberg, S. Li, A. C. Balazs and J. Aizenberg, *Proc. Natl. Acad. Sci. U. S. A.*, 2018, **115**, 12950–12955.

37 T. H. Ware, M. E. McConney, J. J. Wie, V. P. Tondiglia and T. J. White, *Science*, 2015, **347**, 982–984.

38 T. J. White and D. J. Broer, *Nat. Mater.*, 2015, **14**, 1087–1098.

39 A. Buguin, M. Li, P. Silberzan, B. Ladoux and P. Keller, *J. Am. Chem. Soc.*, 2006, **128**, 1088–1089.

40 S. C. Li, M. Aizenberg, M. M. Lerch and J. Aizenberg, *Acc. Mater. Res.*, 2023, **4**, 1008–1019.

41 P. Zhu and L. Wang, *Chem. Rev.*, 2022, **122**, 7010–7060.

42 Q. He, Z. Wang, Y. Wang, Z. Wang, C. Li, R. Annapooranan, J. Zeng, R. Chen and S. Cai, *Sci. Robot.*, 2021, **6**, eabi9704.

43 D. Ditter, P. Blümler, B. Klöckner, J. Hilgert and R. Zentel, *Adv. Funct. Mater.*, 2019, **29**, 1902454.

44 C. L. van Oosten, C. W. Bastiaansen and D. J. Broer, *Nat. Mater.*, 2009, **8**, 677–682.

45 E. K. Fleischmann, H. L. Liang, N. Kapernaum, F. Giesselmann, J. Lagerwall and R. Zentel, *Nat. Commun.*, 2012, **3**, 1178.

46 F. T. Cheng, R. Y. Yin, Y. Y. Zhang, C.-C. Yen and Y. L. Yu, *Soft Matter*, 2015, **6**, 3447–3449.

47 C. L. Huang, J.-A. Lv, X. J. Tian, Y. C. Wang, Y. L. Yu and J. Liu, *Sci. Rep.*, 2015, **5**, 17414.

48 X. L. Lu, H. Zhang, G. X. Fei, B. Yu, X. Tong, H. S. Xia and Y. Zhao, *Adv. Mater.*, 2018, **30**, 1706597.

49 M. P. da Cunha, S. Ambergen, M. G. Debije, E. F. Homburg, J. M. den Toonder and A. P. Schenning, *Adv. Sci.*, 2020, **7**, 1902842.

50 M. O. Saed, A. Gablier and E. M. Terentjev, *Chem. Rev.*, 2021, **5**, 4927–4945.

51 A. H. Gelebart, D. Jan Mulder, M. Varga, A. Konya, G. Vantomme, E. W. Meijer, R. L. B. Selinger and D. J. Broer, *Nature*, 2017, **546**, 632–636.

52 J. A. Lv, Y. Liu, J. Wei, E. Chen, L. Qin and Y. Yu, *Nature*, 2016, **537**, 179–184.

53 L. B. Braun, T. Hessberger and R. Zentel, *J. Mater. Chem. C*, 2016, **4**, 8670–8678.

54 H. K. Bisoyi and Q. Li, *Chem. Rev.*, 2016, **116**, 15089–15166.

55 K. M. Herbert, H. E. Fowler, J. M. McCracken, K. R. Schlafmann, J. A. Koch and T. J. White, *Nat. Rev. Mater.*, 2021, **7**, 23–38.

56 S. Li, M. M. Lerch, J. T. Waters, B. Deng, R. S. Martens, Y. Yao, D. Y. Kim, K. Bertoldi, A. Grinthal, A. C. Balazs and J. Aizenberg, *Nature*, 2022, **605**, 76–83.

57 J. T. Waters, S. C. Li, Y. X. Yao, M. M. Lerch, M. Aizenberg, J. Aizenberg and A. C. Balazs, *Sci. Adv.*, 2020, **6**, eaay5349.

58 C. P. Ambulo, S. Tasmim, S. Wang, M. K. Abdelrahman, P. E. Zimmern and T. H. Ware, *J. Appl. Phys.*, 2020, **128**, 140901.